Materials
Horizons

ROYAL SOCIETY
OF CHEMISTRY

COMMUNICATION

View Article Online
View Journal

Check for updates

Cite this: DOI: 10.1039/d6mh00367b

Received 27th February 2026,
Accepted 13th April 2026

DOI: 10.1039/d6mh00367b

rsc.li/materials-horizons

Unlocking the role of indium ions in stabilizing zinc negative electrodes in highly acidic electrolytes for high-voltage aqueous Zn batteries

Ting-Yu Wang,[a] Hung-Yi Huang,[a] Yi-Heng Tu,[a] Yi-Cheng Liao,[a] Chi-Yu Lai,[a] Timo Jacob,[bcd] Mohamed M. Elnagar,[bcd] Mohammad Al-Shakran[b] and Chi-Chang Hu *[aef]

Operating Zn‖MnO_2 and Zn‖PbO_2 batteries in highly acidic electrolytes enables much higher output voltages (up to *ca.* 2 V and 2.5 V, respectively) than near-neutral systems, making them attractive for high-energy aqueous zinc-ion batteries. However, Zn electrodes suffer from severe hydrogen evolution reaction (HER) and self-corrosion in acidic media, limiting their cycling stability. Here, we introduce indium ions to stabilize Zn electrodes in highly acidic electrolytes. During Zn plating, indium accumulates at the electrode surface to form a protective In–Zn alloy layer, which alleviates the HER by weakening the hydrated proton adsorption and promotes preferential growth of the Zn (002) facet, enabling highly reversible Zn plating/stripping. Moreover, the replacement deposition during rest can generate an indium-containing protection layer that mitigates Zn self-corrosion. Consequently, Zn‖Zn symmetric cells exhibit an extended cycling life approaching 3000 h (at pH 1.13), while acidic Zn‖MnO_2 coin cells deliver a record-high discharge plateau of ~1.95 V with stable cycling over 1100 cycles. Notably, the effectiveness of In^{3+} additives is validated in highly acidic Zn‖PbO_2 batteries, demonstrating their general applicability. This work provides a comprehensive understanding of the In^{3+}-regulated interfacial chemistry for high-voltage Zn batteries in highly acidic electrolytes.

New concepts

In this study, we introduce hydrogen-affinity engineering, a new concept that kinetically suppresses proton-driven parasitic reactions, enabling high-voltage aqueous Zn batteries to operate stably under highly acidic conditions. By enabling stable Zn plating and stripping at pH 1.13, this approach unlocks high-voltage Zn‖MnO_2 (~2.0 V) and Zn‖PbO_2 (~2.35 V) batteries. Unlike conventional strategies that focus on Zn morphology or solvation, our approach employs trace In^{3+} ions to form a self-adaptive, low-hydrogen-affinity interphase, effectively suppressing proton-driven parasitic reactions even in highly acidic electrolytes. Importantly, this strategy operates through two complementary mechanisms: (1) dynamic alloying during galvanostatic cycling and (2) spontaneous replacement deposition under open-circuit conditions, enabling continuous and self-adaptive interfacial protection even during rest. This approach represents a paradigm shift from static protective coatings toward dynamically regenerated, proton-repelling interphases specifically designed for highly acidic environments. By establishing hydrogen-affinity engineering as a general interfacial design principle, this work provides guidance for mitigating proton-induced parasitic reactions in Zn and potentially other proton-sensitive metals, opening new avenues for high-voltage aqueous metal batteries.

1. Introduction

Developing reliable energy storage systems is crucial for enabling large-scale deployment and integration of renewable energy to achieve carbon neutrality. Among various options, aqueous zinc-ion batteries (ZIBs) have emerged as highly promising candidates due to their safety, non-toxicity, low cost, high theoretical capacity (820 mAh g^{-1} for the Zn negative electrode), and excellent stability under ambient conditions.[1–4] Among the numerous positive electrode materials for ZIBs, manganese dioxide (MnO_2) stands out because of its natural abundance, environmental compatibility, and high cell voltage.

Generally, MnO_2 undergoes Zn^{2+} or proton intercalation through a one-electron transfer process in mildly acidic electrolytes, resulting in a relatively low output voltage. To increase both discharge capacity and cell voltage, highly acidic electrolytes have been introduced to activate a two-electron dissolution–deposition mechanism, enabling a remarkable theoretical specific capacity of 616 mAh g^{-1} and a high discharge voltage approaching 2 V (*vs.* Zn^{2+}/Zn).[5,6] Beyond manganese-based

---

[a] *Department of Chemical Engineering, National Tsing Hua University, Hsinchu, 300044, Taiwan. E-mail: cchu@che.nthu.edu.tw*
[b] *Institute of Electrochemistry, Ulm University, Albert-Einstein-Allee 47, 89081, Ulm, Germany*
[c] *Helmholtz-Institute-Ulm (HIU), Helmholtzstr. 11, 89081, Ulm, Germany*
[d] *Karlsruhe Institute of Technology (KIT), P.O. Box 3640, 76021, Karlsruhe, Germany*
[e] *College of Semiconductor Research, National Tsing Hua University, Hsinchu, 300044, Taiwan*
[f] *College of Sustainability, National Tsing Hua University, Hsinchu, 300044, Taiwan*

systems, lead dioxide (PbO_2) is another compelling positive electrode candidate that operates exceptionally well in relatively concentrated H_2SO_4 solutions. By coupling Zn and PbO_2 to construct a Zn‖PbO_2 battery, the theoretical cell voltage can be further elevated to 2.5 V, surpassing that of most ZIBs.[7] This configuration simultaneously exhibits high energy storage performance and improves environmental compatibility by substantially reducing the lead usage relative to conventional lead–acid batteries.[8,9]

However, in highly acidic electrolytes, zinc suffers from vigorous hydrogen evolution reaction (HER) and severe self-corrosion, which substantially shorten the cycling life and raise safety concerns.[10–12] Therefore, suppressing acid-induced corrosion and the HER represents the primary challenge in stabilizing zinc electrodes in highly acidic environments. To address these challenges, several strategies have been proposed, including interfacial protective layers, proton barrier membranes, and battery decoupling designs.[6,13,14] Beyond them, electrolyte additives have attracted increasing attention due to their cost-effectiveness, simplicity, and high efficiency.[15,16] In general, the reported mechanisms of additives fall into two categories: interfacial regulation and solvation structure optimization.[17] The former method utilizes species like ammonium acetate and cerium sulfate to adsorb onto the Zn surface and guide uniform nucleation.[18–20] The latter strategy involves additives, particularly specific anions or polar molecules like dimethyl sulfoxide, that penetrate the Zn^{2+} solvation shell to displace reactive water molecules, thereby minimizing water-induced side reactions.[21–24] However, in highly acidic environments, the primary challenge shifts from merely guiding deposition uniformity to actively suppressing vigorous HER. In such low-pH media, conventional strategies based on physical adsorption or bulk solvation regulation are often insufficient to counteract the high proton activity, because they operate indirectly and do not address the electronic origin of the HER on the Zn surface.[25] Therefore, there is an urgent need to develop additives capable of elevating the HER overpotential at the electrode–electrolyte interface by targeting the electronic origin of the HER.

As a result, this research introduces trace In^{3+} as an electrolyte additive that targets the electronic origin of the HER. Compared with previously reported Zn additives and alloying strategies in acidic electrolytes, these conventional methods still suffer from certain limitations. Many existing additive-based approaches are demonstrated under slightly strong acidic conditions (pH 2–3), and remain less explored at pH $\approx$ 1 required for high-voltage Zn‖PbO_2 batteries. This may constrain their practical applicability in next-generation aqueous Zn systems.[15,26] Conventional alloying strategies can partially address this limitation by extending the stable pH window, but their application is often restricted by the complicated fabrication processes and the potential involvement of toxic materials with environmental concerns.[27,28]

Herein, we introduce In^{3+} as an electrolyte additive that bridges the gap between operational simplicity and robust interfacial protection. We show that indium atoms thermodynamically accumulate at the electrode interface during Zn plating, forming a stable protective indium–zinc binary alloy surface that regulates interfacial reactions and Zn deposition. The indium–zinc binary alloy surface alleviates the HER and other parasitic reactions owing to its low affinity for hydrated protons (H_3O^+), while simultaneously inducing preferential growth of the Zn (002) facet, thereby ensuring highly reversible Zn plating/stripping. The low hydrogen affinity of indium is also evident in the open-circuit state (*i.e.*, resting). During resting, In^{3+} undergoes replacement deposition to form an indium-containing surface layer on the Zn electrode, effectively protecting Zn from self-corrosion. Benefiting from this, the Zn‖Zn symmetric cell containing the In^{3+} additive exhibits an extended cycle life approaching 3000 h in a highly acidic electrolyte (pH = 1.13). Furthermore, the Zn‖MnO_2 coin cells incorporating In^{3+} deliver a high discharge plateau of nearly 1.95 V with stable cycling performance for more than 1100 cycles. In addition, the pouch-cell demonstrations validate the practical feasibility of this design with over 200 cycles. Furthermore, In^{3+} was introduced as an electrolyte additive in a Zn‖PbO_2 battery to evaluate the universality of HER alleviation and self-corrosion inhibition under more stringent electrochemical conditions, which feature a record high discharge plateau of 2.35 V. These findings elucidate the role of In^{3+} additives as the HER and self-corrosion moderators and establish a clear mechanistic framework for their rational deployment in high-voltage aqueous Zn-based batteries.

2. Results and discussion

2.1 Parasitic reaction evolution

Coulombic efficiency (CE) is a key indicator of the reversibility of Zn plating and stripping in aqueous electrolytes.[29,30] The CE loss mainly originates from the parasitic reactions such as the HER and the formation of inactive ("dead") Zn during cycling, both of which undermine long-term stability. Therefore, CE evaluation is essential and it provides a reliable measure of the electrochemical reversibility of the Zn negative electrode and overall electrochemical robustness.[31,32] Firstly, we prepared a highly acidic $ZnSO_4$ electrolyte containing In^{3+} as an additive (denoted as ZSO/In^{3+}). The optimized composition was 5 mM indium sulfate ($In_2(SO_4)_3$, 1 M $ZnSO_4$, and 0.1 M H_2SO_4) in aqueous solutions, according to Fig. S1 and the corresponding discussion. On the other hand, the one without indium sulfate (denoted as ZSO) was studied as a reference electrolyte.

CE was measured during the Zn plating/stripping process in both ZSO/In^{3+} and ZSO electrolytes on the graphite paper at 1 mA cm^{-2} and 1 mAh cm^{-2}. As shown in Fig. 1A and B, the ZSO cell short-circuited within 25 cycles, delivering an accumulated capacity of approximately 22 mAh cm^{-2}, as indicated by the abrupt voltage drop. In stark contrast, the ZSO/In^{3+} cell sustained more than 225 cycles with the accumulated capacity exceeding 230 mAh cm^{-2}. The detailed galvanostatic charge–discharge (GCD) profiles measured at 1 mA cm^{-2} further reveal that the presence of In^{3+} significantly reduces the overpotential of Zn plating/stripping (Fig. 1C and Fig. S2). Specifically, the

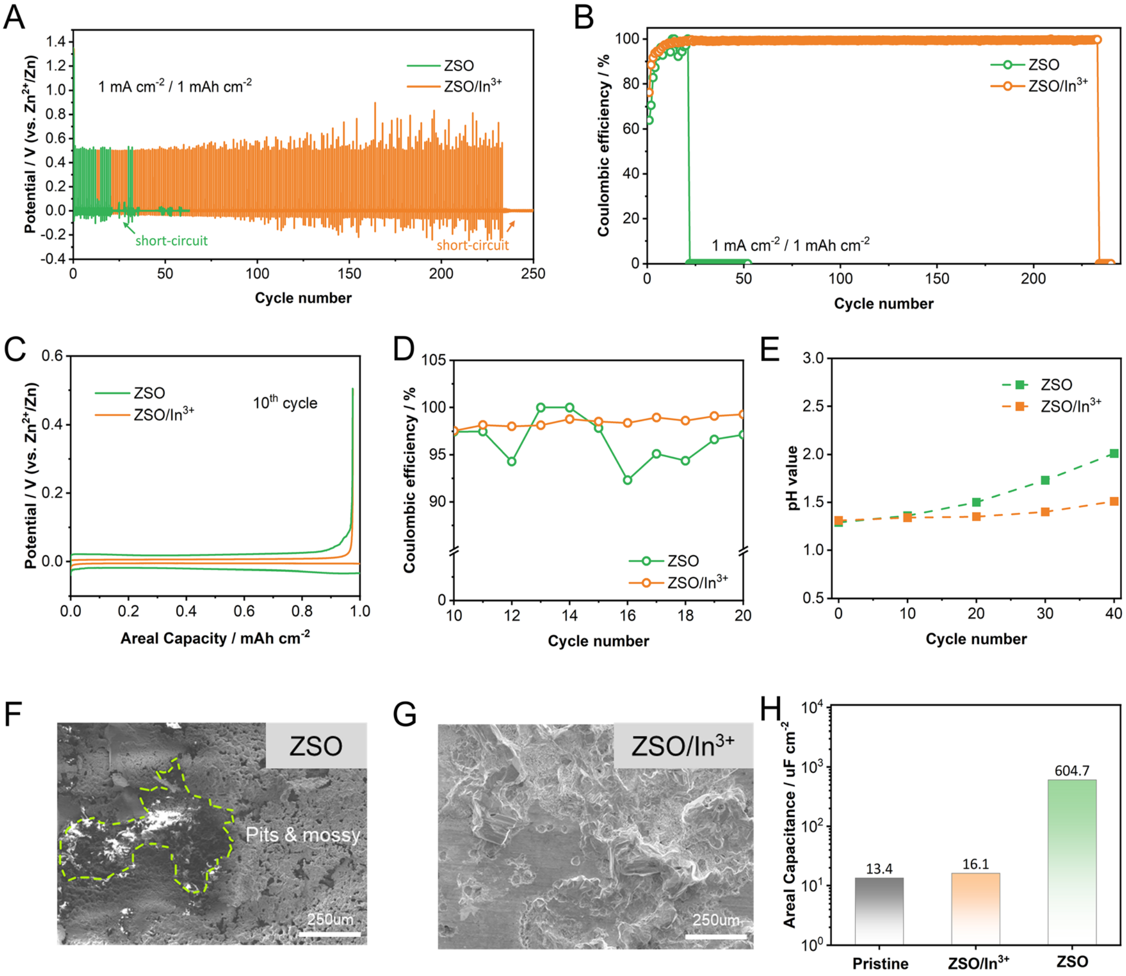

Fig. 1 Effects of In^{3+} additives on the Zn plating/stripping reversibility and HER alleviation. (A) The galvanostatic charge–discharge voltage profiles and (B) corresponding CE of Zn plating/stripping at 1 mA cm^{-2} and 1 mAh cm^{-2} in ZSO and ZSO/In^{3+} electrolytes. (C) Detailed galvanostatic charge–discharge voltage profiles at the 10th cycle. (D) Detailed CE profiles at 1 mA cm^{-2} and 1 mAh cm^{-2}. (E) pH values of Zn‖Zn symmetric cells during cycling. (F) and (G) Optical microscopy images of the Zn electrode after 40 cycles in (F) ZSO and (G) ZSO/In^{3+} electrolytes. (H) Geometric area capacitance of Zn electrodes before and after cycling in ZSO or ZSO/In^{3+} electrolytes.

Zn/In^{3+} cell exhibits a low overpotential of 12.2 mV, compared to the much higher value of 39.1 mV at the 10th cycle observed in the ZSO electrolyte, indicating substantially improved reaction kinetics. Moreover, the CE evolution highlights a pronounced difference in stability. The ZSO cell exhibits highly fluctuating CE behavior, whereas the ZSO/In^{3+} cell maintains a stable CE of nearly 97% throughout cycling (Fig. 1D), highlighting the critical role of In^{3+} in enhancing the reversibility of Zn plating/stripping. Similar trends were observed at a higher current density of 5 mA cm^{-2}, where ZSO/In^{3+} exhibits a higher and much stable CE, compared to ZSO, as shown in Fig. S3.

Notably, in highly acidic electrolytes, the CE loss is often attributed to the parasitic HER which consumes protons and competes with Zn deposition.[15] Motivated by the markedly improved CE in the presence of In^{3+}, we therefore tracked the electrolyte pH during Zn‖Zn cycling as an indirect yet sensitive probe of the HER (Fig. 1E). The ZSO/In^{3+} electrolyte exhibits a minor pH drift, remaining at 1.51 after 40 cycles at 1 mA cm^{-2} and 1 mAh cm^{-2}, while an obvious increase to 2.01 is visible in the ZSO electrolyte (Fig. 1E and the quantitative analysis of the hydrogen evolution rate is provided in Table S1). This observation indicates that the presence of In^{3+} effectively alleviates the HER during cycling. The corresponding optical microscopy (OM) images corroborate this observation, showing distinct morphological differences of Zn obtained in the two electrolytes. The Zn electrode cycled in the ZSO electrolyte for 40 cycles at 1 mA cm^{-2} and 1 mAh cm^{-2} exhibits large surface pits and a pronounced mossy morphology (Fig. 1F), whereas the Zn electrode cycled in the ZSO/In^{3+} electrolyte displays a compact and uniform surface (Fig. 1G). To further quantify the surface evolution, the geometric area capacitance of both Zn electrodes was measured in 1 M Na_2SO_4 to exclude the faradaic contributions from the Zn deposition and HER in order to precisely determine the double-layer capacitance.[33–35] Since the double-layer capacitance is proportional to the accessible electrode surface area, changes in geometric area capacitance reflect variations in surface roughness, porosity, or morphological features during cycling. Therefore, the geometric area capacitance is considered a reliable and quantitative indicator of electrode surface area. As shown in Fig. 1H (with detailed calculation in Fig. S4), the geometric area capacitance of the Zn electrode cycled in the ZSO electrolyte increased by approximately 45-fold after 20 h of cycling (604.7 μF cm^{-2}) compared to the pristine Zn electrode (13.4 μF cm^{-2}), whereas the Zn electrode cycled in the ZSO/In^{3+} electrolyte exhibited a negligible variation (16.1 μF cm^{-2}), indicating that the In^{3+} additives effectively alleviate the surface roughening and stabilize the Zn surface. Importantly, the much lower geometric area capacitance reflects a much smaller electrochemically active surface area, thereby reducing the number of accessible sites for proton reduction and effectively alleviates the HER and improving the overall electrochemical reversibility of the Zn electrode.[36]

2.2 Electrochemical properties of the zinc electrode with indium additives

To directly evaluate the effect of In^{3+} additives on the intrinsic reversibility and cycling stability of the Zn electrode, symmetric Zn‖Zn cells were evaluated in ZSO and ZSO/In^{3+} at 1 mA cm^{-2} with an areal capacity of 1 mAh cm^{-2} (Fig. 2A and Fig. S5). Without In^{3+}, the ZSO symmetric cell short-circuited after about 60 h cycling, indicating rapid interfacial degradation. Strikingly, introducing In^{3+} into the same electrolyte enabled the stable cycling for nearly 3000 h, representing an improvement of nearly 50-fold in cycle life. This dramatic enhancement originates from

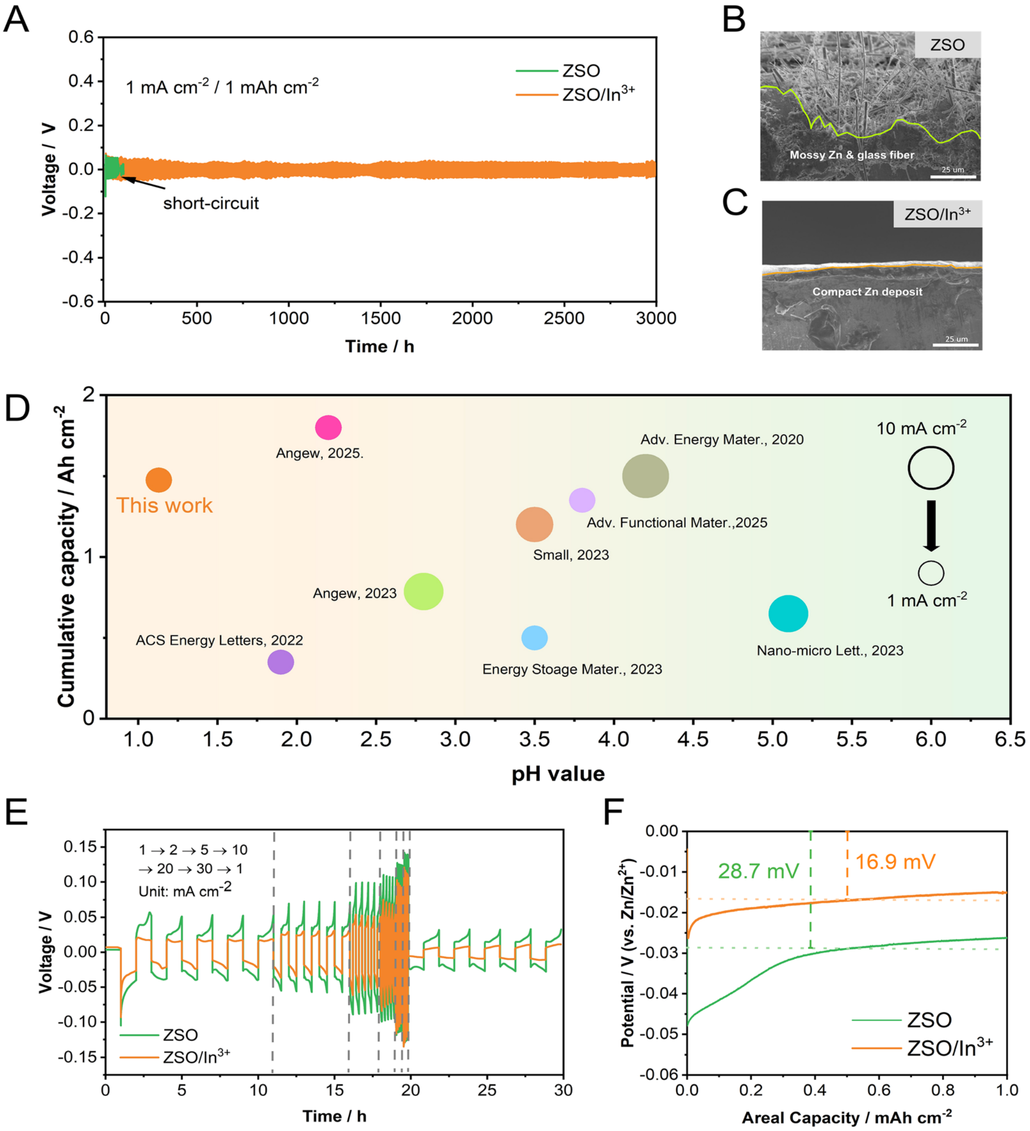

Fig. 2 Long-term reversibility and rate capability of Zn symmetric cells. (A) Cycling stability of ZSO and ZSO/In^{3+} symmetric cells operated at 1 mA cm^{-2} with an areal capacity of 1 mAh cm^{-2}. (B) and (C) The optical microscopy images of the Zn electrode after 100 h in (B) ZSO and (C) ZSO/In^{3+} electrolytes. (D) Electrochemical performance of the symmetric cells compared to the state-of-the-art works in the literature.[6,38–44] (E) Galvanostatic voltage profiles of these symmetric cells at various current densities (1, 2, 5, 10, 20, 30, and 1 mA cm^{-2}). (F) Galvanostatic voltage profiles of a three-electrode system in ZSO and ZSO/In^{3+} at 1 mA cm^{-2} during the Zn plating process.

the In^{3+}-regulated Zn deposition behavior. SEM images of the Zn electrodes after the 100 h cycling test in ZSO and ZSO/In^{3+} reveal the morphology difference between two electrodes, where the one in ZSO exhibits a mossy deposit (Fig. 2B) and the electrode in ZSO/In^{3+} remains smooth and compact (Fig. 2C). Such compact deposition indicates the improved reversibility of Zn plating and stripping, which directly contributes to the extended cycle life.[30,37] These results are in good agreement with the previously observed high and stable coulombic efficiency obtained in ZSO/In^{3+}, which reflects the enhanced reversibility of Zn plating and stripping. Fig. 2D and Table S2 compare the performance of our Zn‖Zn symmetric cell using ZSO/In^{3+} with state-of-the-art Zn‖Zn symmetric cells. In summary, the system using ZSO/In^{3+} not only operates at a relatively low pH but also maintains high cumulative capacities, setting a new benchmark for Zn symmetric cells in highly acidic electrolytes ($pH < 2$).

The rate capability and electrode kinetics of Zn in ZSO/In^{3+} under various operating conditions were tested at current densities ranging from 1 to 30 mA cm^{-2}. The voltage hysteresis of the cell using ZSO/In^{3+} remains consistently lower than that of the cell using ZSO across the tested current densities (Fig. 2E), indicating smaller polarization at the electrode/electrolyte interface. This observation is consistent with the reduced overpotential seen in Fig. 1C and Fig. S2, reflecting better Zn plating and stripping kinetics in the presence of In^{3+} ions.

A three-electrode system was employed to separately evaluate the polarization behavior during the Zn stripping and plating processes. During the stripping process under anodic current, the polarization voltage in the ZSO electrolytes decreases from 32.7 mV to 26.2 mV after the introduction of In^{3+}, corresponding to a voltage reduction of 6.5 mV (Fig. S6). In contrast, during the plating process under cathodic current, the polarization voltage is reduced from 28.7 mV in ZSO to 16.9 mV in ZSO/In^{3+} electrolytes, yielding a larger decrease of 11.8 mV (Fig. 2F). These results indicate that indium incorporation alleviates the polarization in both Zn stripping and plating processes, while the improvement in polarization behavior is primarily associated with the Zn plating process, where the reduced cathodic polarization reflects a lower nucleation and growth barrier.

2.3 *In situ* formation of the In–Zn binary alloy protective layer

Given the pronounced stabilization of Zn electrodes enabled by In^{3+} additives in highly acidic electrolytes, the underlying mechanism in the electrochemical process needs to be elucidated. It is necessary to clarify whether In^{3+} acts solely as the dissolved

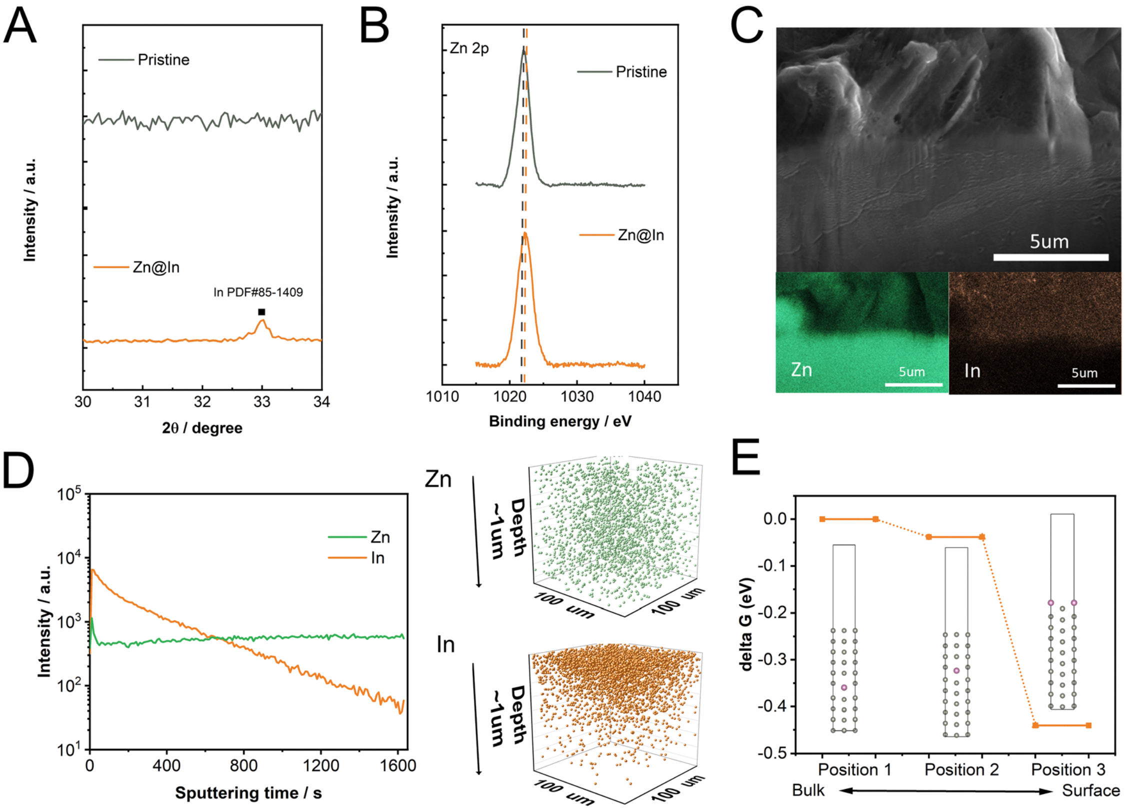

Fig. 3 Indium co-deposition and binary alloy formation on Zn electrodes. (A) XPS spectra of Zn 2p for pristine Zn and Zn@In electrodes. (B) Enlarged XRD patterns of pristine Zn and Zn@In electrodes. (C) Cross-sectional FIB–SEM–EDS elemental mapping of a Zn deposit prepared in the ZSO electrolyte containing 50 mM indium sulfate. (D) The TOF-SIMS depth profiles and corresponding three-dimensional distributions of Zn and In within the sputtered volume of the Zn@In electrode. (E) Gibbs free energies of indium at three positions within the Zn lattice. The purple and gray spheres represent indium and zinc atoms, respectively.

electrolyte additive that regulates the interfacial reactions, or it is incorporated into the Zn electrode through co-deposition for alloy formation. To address this issue, a Zn@In electrode was prepared by galvanostatic plating in the ZSO/In^{3+} electrolyte at a current density of 1 mA cm^{-2} with an areal capacity of 1 mAh cm^{-2}. XRD patterns first reveal the appearance of an indium diffraction peak at $\sim$32.9°, which is absent in pristine Zn, indicating the formation of metallic indium (Fig. 3A and Fig. S7).[45] This observation is further confirmed by XPS analysis which shows distinct In 3d signals on the Zn surface that are completely absent in pristine Zn (Fig. S8). Meanwhile, the Zn 2p peaks exhibit a positive shift of approximately 0.2 eV, moving from 1022.0 eV for pristine Zn to 1022.2 eV for Zn@In (Fig. 3B), indicating significant interaction between Zn and In.[46] In addition, the surface composition quantified by XPS (Table S3) indicates a Zn-to-In ratio within the In–Zn solid solution region, further confirming the possible formation of the In–Zn alloy upon introduction of In^{3+} additives (Fig. S9).[47,48]

FIB–SEM–EDS analysis was conducted to investigate the depth-spatial distribution of indium within the deposits, revealing a pronounced surface enrichment of indium on the Zn deposits as shown in Fig. 3C. TOF-SIMS analysis was further employed to provide a more detailed assessment of the depth-dependent distribution of indium. Fig. 3D demonstrates the TOF-SIMS profiles and the corresponding three-dimensional spatial distribution of indium. These results reveal a clear gradient distribution of indium, with the highest concentration near the electrolyte/electrode interface and gradually decreasing with depth over approximately 1 μm. Notably, indium signals are still detectable within the Zn deposits, indicating that indium is incorporated throughout the Zn deposition process, rather than only appearing on the surface due to replacement deposition between Zn atoms and In ions at the electrolyte/electrode interface. Collectively, these results indicate that indium participates in the electrochemical process predominantly through co-deposition with Zn, forming the alloyed interfacial layer rather than remaining only in the electrolyte. To elucidate the thermodynamic origin for the gradient distribution of indium, DFT calculations were performed to evaluate the Gibbs free energy of indium atoms at different positions within the Zn lattice (Fig. 3E). Indium in the bulk (position 1) was taken as the reference (0 eV), while positions closer to the surface exhibited lower Gibbs free energies of −0.038 eV at position 2 and −0.44 eV at the surface (position 3). These results indicate that indium atoms residing at the Zn surface exhibit the lowest Gibbs free energy, thereby thermodynamically favoring the indium surface segregation during Zn plating, which may contribute to alleviating the parasitic reactions.

2.4 The hidden role of In ions

To investigate whether the formation of an In-containing surface can effectively alleviate the HER on the zinc electrode, linear sweep voltammetry (LSV) was performed in 0.1 M H_2SO_4 to evaluate the HER activity of pristine Zn and Zn@In electrodes.[10,49] As shown in Fig. 4A, the pristine Zn electrode exhibits a pronounced increase in cathodic current associated with the HER, while the Zn@In electrode shows a significantly lower current throughout the sweep. This reduced current response indicates that the In-containing surface provides the improved resistance against the HER, the main parasitic reaction on the Zn electrode. The observed HER alleviation can be understood from the perspective of metal–adsorbed H atom interactions that govern the HER activity. According to Sabatier's principle for effective HER metal catalysts, the binding strength between metallic catalyst atoms and adsorbed H atoms (intermediates) must be neither too strong nor too weak.[50] For metals such as In and Cd, weak hydrogen binding limits the Volmer step, leading to a lower HER exchange current density.[51] The density functional theory (DFT) further supports this HER alleviation mechanism. When indium is present on the Zn surface, the Zn@In surface exhibits a weaker binding energy toward hydrated protons (−18.1 eV) compared to pristine Zn (−25.8 eV), indicating that H_3O^+ adsorption is energetically less favorable on Zn@In (Fig. 4B). This reduced affinity for hydrated protons accounts for the alleviated HER activity and highlights the critical role of the In-containing surface as a HER-unfavorable protective layer in stabilizing the Zn electrode. Notably, this behavior is consistent with Trassati's volcano plot for the HER in acidic solutions (Fig. S10).[52,53]

On the other hand, this enhanced HER alleviation arises not only from the formation of an In-containing surface but also from the preferential growth of the Zn (002) facet, which is intrinsically less active toward the HER.[54,55] X-ray diffraction (XRD) analysis of Zn electrodes after cycling in ZSO and ZSO/In^{3+} reveals such facet-selective behavior. The relative texture coefficients (RTCs) calculated from the XRD patterns show that Zn electrodes cycled in the ZSO electrolyte exhibit an RTC of 30.3% for the (002) plane after 40 cycles. In contrast, the Zn electrode cycled in the ZSO/In^{3+} electrolyte displays a markedly an increased Zn (002) texture, with the corresponding RTC rising to 43.2% after cycling (see Fig. 4C and Fig. S11 for calculation details). Such facet-directed growth alleviates the HER and promotes the more reversible Zn plating/stripping.

The adsorption preference of indium atoms on various Zn crystal facets was also calculated through DFT (Fig. 4D). The results reveal a pronounced facet-dependent adsorption energy, in which indium binds strongly to Zn (100), Zn (101), and Zn (102) surfaces, with binding energies of −1.14, −1.22, and −1.23 eV, respectively, whereas its interaction with the Zn (002) facet is considerably weaker (−0.40 eV). This strong facet-selective adsorption indicates that indium atoms preferentially accumulate on Zn (100), Zn (101), and Zn (102) planes, which are widely recognized to be catalytically active toward the HER.[55,56] As a result, indium provides more effective passivation and protection for these HER-prone facets, thereby alleviating the parasitic HER and improving the interfacial stability of the Zn electrode.

In practical batteries, the Zn electrodes often experience rest periods without applied currents, during which severe self-corrosion commonly occurs due to the H^+ adsorption and electron transfer at the metal surface in such an acidic environment.[57,58] Therefore, evaluating the corrosion resistance under the

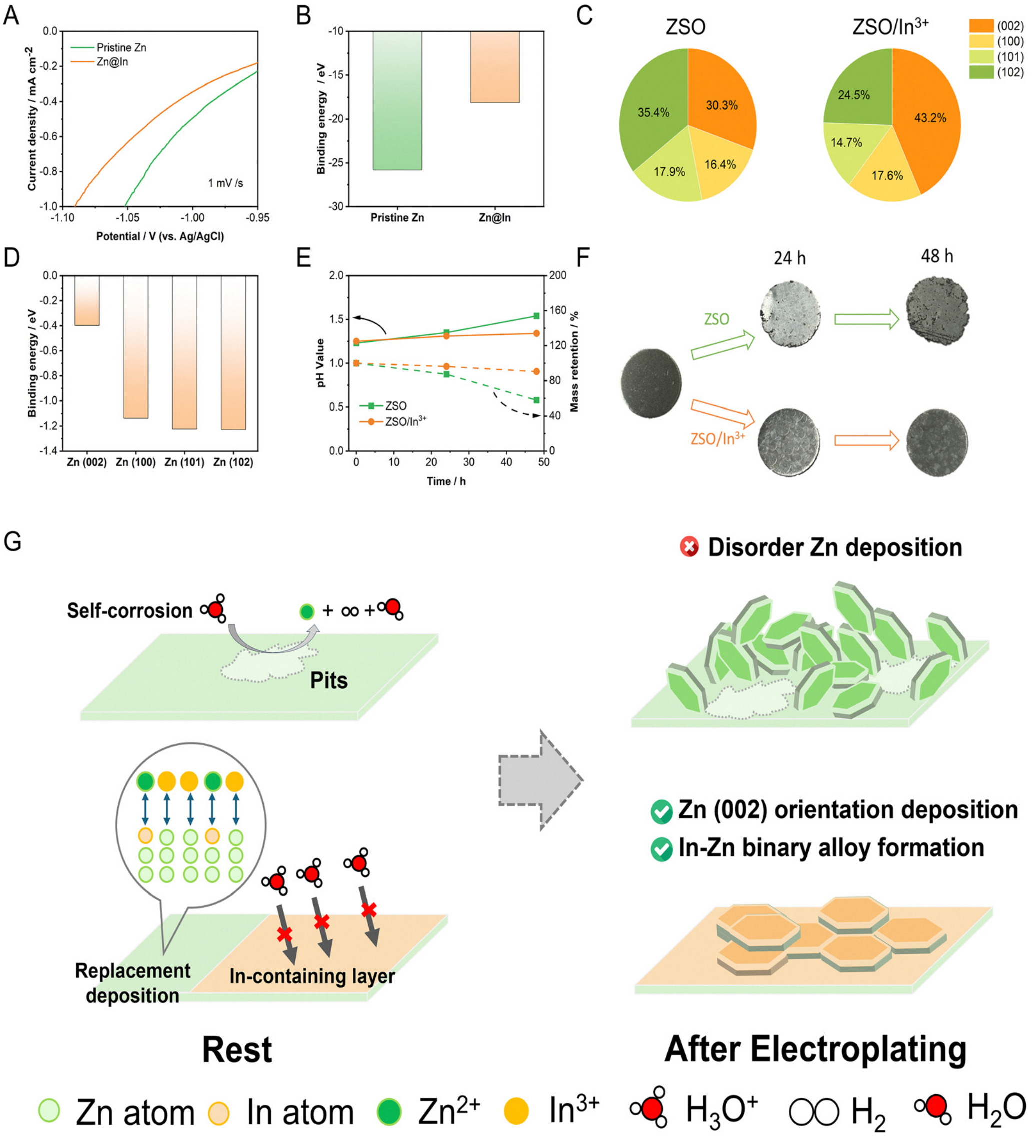

Fig. 4 (A) LSV curves of pristine Zn and Zn@In electrodes measured at 1 mV s^{-1} in 0.1 M H_2SO_4. (B) The binding energy of H_3O^+ on the pristine Zn and Zn@In surfaces. (C) The RTC values of Zn electrodes after 40 cycles in ZSO and ZSO/In^{3+} electrolytes. (D) The binding energy of indium atoms on various Zn crystal facets. (E) The pH values and mass retention of zinc foils immersed in ZSO and ZSO/In^{3+} electrolytes and (F) the corresponding OM images of Zn electrodes. (G) A schematic diagram of Zn resting and electroplating processes in ZSO and ZSO/In^{3+} electrolytes.

open-circuit condition is essential to ensure the electrode stability during these rest periods. To this end, Zn foils were immersed in ZSO and ZSO/In^{3+} electrolytes, respectively, and the variations in both pH and mass were periodically monitored. The Zn foil immersed in the ZSO electrolyte exhibited a pronounced decrease in mass, retaining only 57.8% of their initial mass after 48 h. On the other hand, the one in the ZSO/In^{3+} electrolyte maintained 90.5% of its initial mass (Fig. 4E and the quantitative analysis of self-corrosion rate is provided in Table S4), providing the evidence consistent with corrosion alleviation in the presence of In^{3+}. Consistent results were obtained from pH monitoring which revealed the significant reduction in pH change in the presence of In^{3+}.

The optical microscopy (OM) results further highlighted the differences in surface morphology, as shown in Fig. 4F. The Zn foil in the basic electrolyte became severe roughening after 48 h, indicative of the extensive acidic corrosion, while the Zn foil in the ZSO/In^{3+} electrolyte maintained smooth and intact surfaces. These observations indicate that the introduction of indium ions alleviates the self-corrosion even during simple soaking without applied current. This alleviation is likely associated with the formation of indium-containing surface species which possibly mitigate the Volmer step of the HER owing to the weaker hydrogen binding affinity of indium compared with Zn metal. The formation of this indium-containing surface can be rationalized by a spontaneous replacement deposition process between Zn and In^{3+}. This replacement deposition originates from the more positive redox potential of the In/In^{3+} couple (−0.34 V *vs.* SHE) compared with that of Zn/Zn^{2+} (−0.76 V *vs.* SHE), which thermodynamically enables the galvanic displacement of surface

Zn atoms by indium species even in the open-circuit state.[59] The presence of indium species is further supported by the XPS analysis, which reveals the distinct In 3d signals on the Zn surface after soaking (Fig. S12).

Overall, these results indicate that In^{3+} stabilizes the Zn surface *via* multiple possible mechanisms: (i) passivation of the HER-prone facets in the open-circuit state *via* replacement deposition to effectively alleviating Zn corrosion and (ii) the *in situ* formation of an In–Zn binary alloy that can lower the hydrated proton activity and guides Zn (002)-oriented growth to promote the reversible Zn plating/stripping, as illustrated in Fig. 4G.

2.5 Full cell performance

In order to demonstrate the practical application of indium additives in a highly acidic environment, a MnO_2-free acidic Zn‖MnO_2 battery (AZMBs) was employed, in which MnO_2 is *in situ* deposited on a bare carbon substrate (MnO_2-free) during the initial cycles in an electrolyte composed of 1 M $ZnSO_4$, 1 M $MnSO_4$, and 0.3 M H_2SO_4 (pH = 0.4) with or without 5 mM indium sulfate. The assembled AZMBs operated in both electrolytes exhibit a typical galvanostatic discharge platform associated with the Mn^{2+}/MnO_2 redox couple. Notably, the AZMB in the ZSO/In^{3+} electrolyte delivers an impressive discharge plateau of ∼2.0 V at 1 mA cm^{-2} and 1.48 V at 30 mA cm^{-2}, which is markedly higher than that in the ZSO electrolyte (1.89 V at 1 mA cm^{-2} and 1.11 V at 30 mA cm^{-2}), as shown in Fig. 5A and B. This performance advantage is further highlighted in the comparison of plateau cell voltages across a wide range of current densities, where the ZSO/In^{3+} cell consistently maintains a higher discharge plateau than the ZSO system (Fig. 5C).

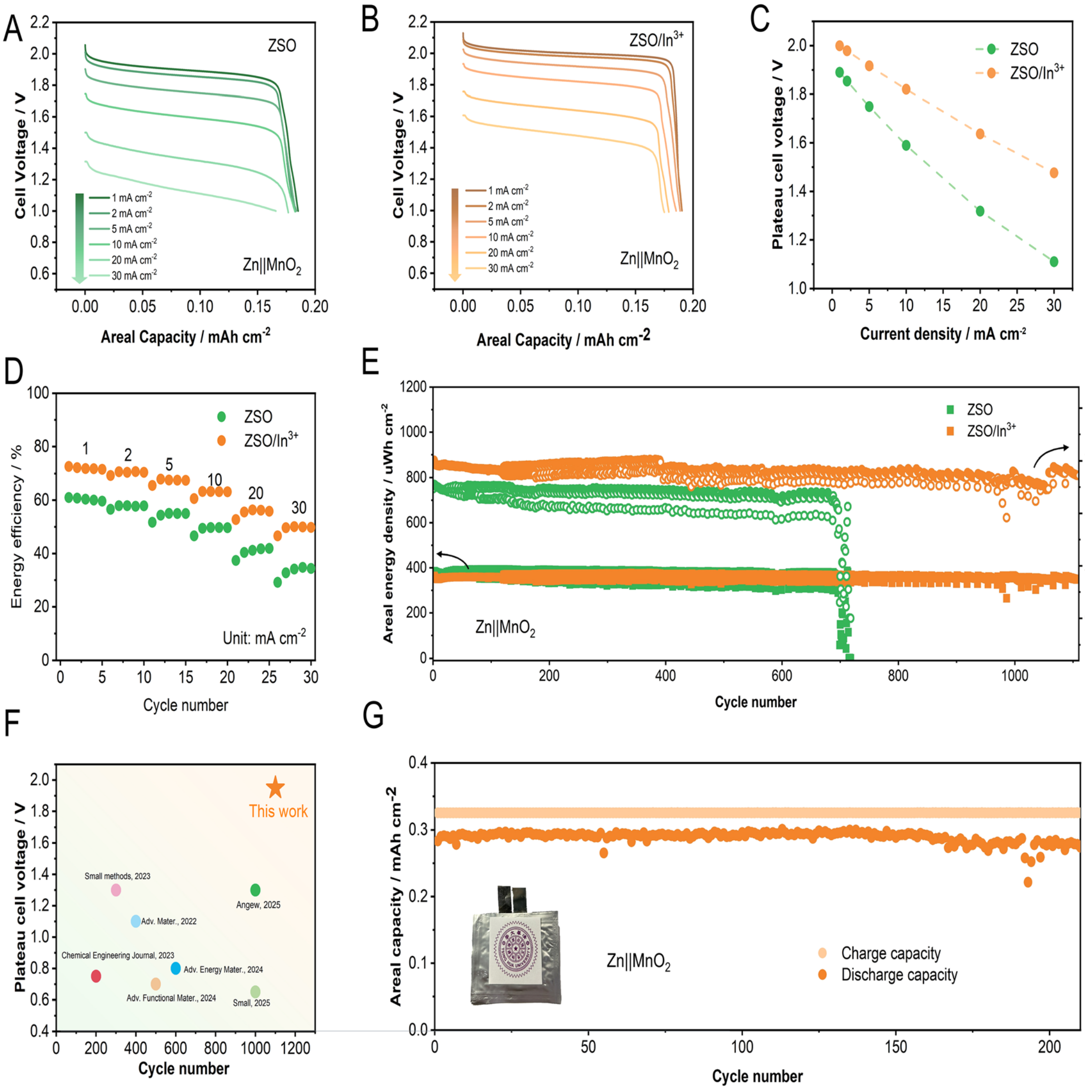

Fig. 5 Performance of AZMBs with the ZSO and ZSO/In^{3+} electrolytes. Galvanostatic discharge profiles of the AZMBs with the (A) ZSO and (B) ZSO/In^{3+} electrolytes across various discharge current densities. (C) Comparisons of plateau cell voltages and (D) energy efficiency of AZMBs in ZSO and ZSO/In^{3+} electrolytes at various current densities.[62–68] (E) Cycling stability of a Zn‖MnO_2 coin cell at 5 mA cm^{-2}. (F) Electrochemical performance of AZMBs with ZSO/In^{3+} and other reported electrolyte additives. (G) Cycling stability of an acidic Zn‖MnO_2 pouch cell at a discharge current density of 5 mA cm^{-2} with an areal capacity of 0.325 mAh cm^{-2}.

Energy efficiency (EE) is a key metric for evaluating battery performance because it represents the fraction of input energy that is effectively converted into usable electrical energy. A high EE indicates that the charging–discharging processes are extremely reversible, with minimal energy loss due to side reactions such as the HER in AZMBs.[60,61] Consistently, the AZMB operated in the ZSO/In^{3+} electrolyte exhibits a superior energy efficiency across all tested current densities (Fig. 5D), reflecting the extremely high reversibility and suppressed parasitic reactions.

Cycling stability performance is displayed in Fig. 5E and Fig. S13. The cell using ZSO/In^{3+} demonstrates excellent durability, maintaining stable cycling for over 1100 cycles at a discharge current density of 5 mA cm^{-2} with an outstanding voltage platform of 1.95 V. In contrast, the one with ZSO shows severe voltage fluctuations and fails in fewer than 700 cycles, primarily due to the pronounced HER occurring at the Zn electrode. Notably, the achieved plateau cell voltage of 1.95 V combined with a cycle life of 1100 cycles surpasses most previously reported aqueous ZIBs (Fig. 5F and Table S5).

Pouch cells were assembled to further evaluate the practical performance of the AZMB using ZSO/In^{3+}. Such a pouch cell sustains 200 cycles with an average discharge areal capacity of 0.325 mA h cm^{-2}, demonstrating its promising potential for practical applications (Fig. 5G).

This HER and self-corrosion alleviation effect of In^{3+} additives is equally effective under the highly acidic conditions required for PbO_2 conversion chemistry. The Zn‖PbO_2 cell was assembled in 1 M $ZnSO_4$ + 2 M H_2SO_4 with or without 5 mM indium sulfate (pH ≈ 0.1). The cell employing ZSO/In^{3+} maintains over 90% EE for 50 cycles, while the one with the ZSO electrolyte shows a lower EE and failed after only 16 cycles (Fig. S14). In addition, the former cell displays a stable high-voltage discharge plateau of 2.35 V at the first cycle, compared to 2.22 V in the cell using the ZSO electrolyte (Fig. S15).

Overall, the introduction of In^{3+} additives broadens the pH stability window of aqueous Zn-based batteries by alleviating the HER and self-corrosion of the Zn electrode in the highly acidic media, enabling the construction of high-voltage batteries.

3. Conclusions

In summary, we demonstrate that incorporating In^{3+} additives effectively stabilizes the Zn negative electrode in highly acidic electrolytes through multiple mechanisms. The formation of an indium-containing interfacial layer *via* replacement deposition passivates the HER-prone facets to mitigate the self-corrosion in the open-circuit state. The formation of a protective In–Zn binary alloy layer on the Zn surface alleviates the HER under plating. Moreover, In^{3+} can guide the preferential growth of Zn along the (002) orientation. These integrated and synergistic mechanisms uniquely promote the Zn plating/stripping reversibility. As a result, the Zn‖Zn symmetric cell exhibits an extended cycling life approaching 3000 h, and the acidic Zn‖MnO_2 coin cell perfectly delivers a high discharge plateau of nearly 1.95 V with stable performance over 1100 cycles. Furthermore, the pouch-cell demonstration with over 200 cycles confirms the practical feasibility of this strategy. Notably, the effectiveness of In^{3+} additives is further validated in highly acidic Zn‖PbO_2 conversion-type batteries, confirming the general applicability of this strategy under extreme environments. Collectively, these findings highlight the effectiveness of In^{3+} additives in enabling highly reversible Zn plating/stripping and provide a clear framework for their application in acidic Zn‖MnO_2 and Zn‖PbO_2 batteries with high discharge plateaus and long-term stability.

Author contributions

Ting-Yu Wang: conceptualization, investigation, writing – review and editing, software, data curation, supervision, writing – original draft, methodology, validation, project administration, visualization, resources, and formal analysis; Hung-Yi Huang: conceptualization, methodology, data curation, investigation, validation, visualization, and writing – review and editing; Yi-Heng Tu: writing – review and editing, conceptualization, methodology, data curation, investigation, and validation; Yi-Cheng Liao: conceptualization, methodology, and writing – review and editing; Chi-Yu Lai: writing – review and editing, investigation, and methodology; Timo Jacob: resources, funding acquisition, and project administration; Mohamed M. Elnagar: data curation, conceptualization, and methodology; Mohammad Al-Shakran: resources and formal analysis; Chi-Chang Hu: funding acquisition, writing – review and editing, methodology, supervision, resources, project administration, and validation.

Conflicts of interest

There are no conflicts of interest to declare.

Data availability

The data that support the findings of this study are available in the supplementary information (SI). XPS; XRD; ECSA; and detailed data in table form. See DOI: https://doi.org/10.1039/d6mh00367b.

Acknowledgements

The financial support of this work by the National Science and Technology Council (NSTC) of Taiwan under contract no. NSTC 114-2221-E-007-013-MY3, NSTC 113-2923-E-007-007-MY3, NSTC 113-2823-8-007-003, NSTC 112-2622-E-007-032, NSTC 112-2223-E-007-006-MY3, NSTC 112-2221-E-007-081, and NSTC 112-2221-E-007-021-MY3 and assistance from Ms Shiou-Ling Lei (instrumentation Center at NTHU) for Time-of-Flight Secondary Ion Mass Spectrometer are gratefully acknowledged.

References

1 Z. Liu, M. Qin, B. Fu, M. Li, S. Liang and G. Fang, *Angew. Chem.*, 2025, **137**, e202417049.

2 Y. Song, M. Chen, Z. Zhong, Z. Liu, S. Liang and G. Fang, *Nat. Commun.*, 2025, **16**, 3142.
3 C.-Y. Lai, K.-Y. Tseng, W.-Y. Jao, T.-Y. Wang, Z.-F. He, Y.-L. Chen, H.-Y. Chen and C.-C. Hu, *Small*, 2025, **21**, e06178.
4 S. Uemura, C. Elkort, K. Than, S. Rapier, Y. Katsuyama, J. Hui, Z. Yang, H.-Y. Huang, C.-C. Hu, M. F. El-Kady and R. B. Kaner, *Small*, 2026, e14911.
5 D. Chao, W. Zhou, C. Ye, Q. Zhang, Y. Chen, L. Gu, K. Davey and S.-Z. Qiao, *Angew. Chem., Int. Ed.*, 2019, **58**, 7823–7828.
6 H. Yang, L. Li, D. Chen, J. Wang, Y. Tan, Z. Jiang, Y. Zhang, C. Miao, W. Zhang and W. Han, *Angew. Chem.*, 2025, **137**, e202419394.
7 Y. Xu, P. Cai, K. Chen, Y. Ding, L. Chen, W. Chen and Z. Wen, *Angew. Chem., Int. Ed.*, 2020, **59**, 23593–23597.
8 J. Liu, Z. Bao, Y. Cui, E. J. Dufek, J. B. Goodenough, P. Khalifah, Q. Li, B. Y. Liaw, P. Liu, A. Manthiram, Y. S. Meng, V. R. Subramanian, M. F. Toney, V. V. Viswanathan, M. S. Whittingham, J. Xiao, W. Xu, J. Yang, X.-Q. Yang and J.-G. Zhang, *Nat. Energy*, 2019, **4**, 180–186.
9 D. Xu, H. Zhang, J. Xie, L. Zhou, F. Yang, J. Ma, Y. Yu, G. Wang and X. Lu, *Adv. Mater.*, 2024, **36**, 2408067.
10 C.-Y. Lai, Y.-S. Liao, H.-Y. Ku, W.-Y. Jao, S. Gull, H.-Y. Chen, J.-P. Chou and C.-C. Hu, *Small*, 2024, **20**, 2401713.
11 J. Chen, W. Zhao, J. Jiang, X. Zhao, S. Zheng, Z. Pan and X. Yang, *Energy Storage Mater.*, 2023, **59**, 102767.
12 X. Yu, Z. Li, X. Wu, H. Zhang, Q. Zhao, H. Liang, H. Wang, D. Chao, F. Wang, Y. Qiao, H. Zhou and S.-G. Sun, *Joule*, 2023, **7**, 1145–1175.
13 Y.-f Cui, Z.-b Zhuang, Z.-l Xie, R.-f Cao, Q. Hao, N. Zhang, W.-q Liu, Y.-h Zhu and G. Huang, *ACS Nano*, 2022, **16**, 20730–20738.
14 C. Zhong, B. Liu, J. Ding, X. Liu, Y. Zhong, Y. Li, C. Sun, X. Han, Y. Deng, N. Zhao and W. Hu, *Nat. Energy*, 2020, **5**, 440–449.
15 Y. Liu, Z. Liu, Z. Xiao, Z. Lao, J. Liu, X. Xiao, Q. Fu, F. Zheng and G. Zhou, *Angew. Chem., Int. Ed.*, 2025, **64**, e202502896.
16 Q. Nian, X. Zhang, Y. Feng, S. Liu, T. Sun, S. Zheng, X. Ren, Z. Tao, D. Zhang and J. Chen, *ACS Energy Lett.*, 2021, **6**, 2174–2180.
17 J. Wan, R. Wang, Z. Liu, L. Zhang, F. Liang, T. Zhou, S. Zhang, L. Zhang, Q. Lu, C. Zhang and Z. Guo, *ACS Nano*, 2023, **17**, 1610–1621.
18 C. Lin, X. Yang, P. Xiong, H. Lin, L. He, Q. Yao, M. Wei, Q. Qian, Q. Chen and L. Zeng, *Adv. Sci.*, 2022, **9**, 2201433.
19 Y. Li, P. Wu, W. Zhong, C. Xie, Y. Xie, Q. Zhang, D. Sun, Y. Tang and H. Wang, *Energy Environ. Sci.*, 2021, **14**, 5563–5571.
20 A. Bayaguud, X. Luo, Y. Fu and C. Zhu, *ACS Energy Lett.*, 2020, **5**, 3012–3020.
21 N. Wang, S. Zhai, Y. Ma, X. Tan, K. Jiang, W. Zhong, W. Zhang, N. Chen, W. Chen, S. Li, G. Han and Z. Li, *Energy Storage Mater.*, 2021, **43**, 585–594.
22 L. Cao, D. Li, E. Hu, J. Xu, T. Deng, L. Ma, Y. Wang, X.-Q. Yang and C. Wang, *J. Am. Chem. Soc.*, 2020, **142**, 21404–21409.
23 Q. Zhang, Y. Ma, Y. Lu, X. Zhou, L. Lin, L. Li, Z. Yan, Q. Zhao, K. Zhang and J. Chen, *Angew. Chem., Int. Ed.*, 2021, **60**, 23357–23364.
24 W. Zhang, J. Chen, C. Guan, T. Qiu, X. Shi, R. Chen, Z. Jiang, Q. Fu, X. Wu, H. Yang, M. Liu, P. Jiang, Y. Zhong, J. Zhou and G. He, *Angew. Chem., Int. Ed.*, 2025, **64**, e202516282.
25 C. Gao, Z. Jiang, J. Chen, K. Zhang, H. Yang, R. Chen, H. Yang, Q. Fu, Z. Li, N. Xu, M. Wang, B. Hong, F. Wu, W. Zhang and Y. Lai, *Sci. Bull.*, 2026, **71**, 1093–1102.
26 H. Yang, L. Li, D. Chen, J. Wang, Y. Tan, Z. Jiang, Y. Zhang, C. Miao, W. Zhang, W. Han and G. He, *Angew. Chem.*, 2025, **137**, e202419394.
27 J. Sun, X. Zheng, K. Li, G. Ma, T. Dai, B. Ban, Y. Yuan, M. Wang, M. Chuai, Y. Xu, Z. Liu, T. Jiang, Z. Zhu, J. Chen, H. Hu and W. Chen, *Energy Storage Mater.*, 2023, **54**, 570–578.
28 P. Ruan, X. Chen, L. Qin, Y. Tang, B. Lu, Z. Zeng, S. Liang and J. Zhou, *Adv. Mater.*, 2023, **35**, 2300577.
29 L. Ma, M. A. Schroeder, O. Borodin, T. P. Pollard, M. S. Ding, C. Wang and K. Xu, *Nat. Energy*, 2020, **5**, 743–749.
30 J. Zheng, Q. Zhao, T. Tang, J. Yin, C. D. Quilty, G. D. Renderos, X. Liu, Y. Deng, L. Wang, D. C. Bock, C. Jaye, D. Zhang, E. S. Takeuchi, K. J. Takeuchi, A. C. Marschilok and L. A. Archer, *Science*, 2019, **366**, 645–648.
31 Z. Wu, Y. Li and J. Liu, *Small Methods*, 2024, **8**, 2300660.
32 W.-Y. Jao, A. Aggarwal, T. K. Telmasre, L. Mishra, V. R. Subramanian, C.-C. Hu and K. J. X. Zheng, *J. Am. Chem. Soc.*, 2026, **148**, 756–765.
33 J. Nan, H. Liu, W. Li, F. Zhao, L. Zhu, H. Chen and W. Li, *ACS Omega*, 2022, **7**, 41013–41020.
34 C. C. L. McCrory, S. Jung, J. C. Peters and T. F. Jaramillo, *J. Am. Chem. Soc.*, 2013, **135**, 16977–16987.
35 S. Trasatti and O. A. Petrii, *Pure Appl. Chem.*, 1991, **63**, 711–734.
36 L. Ren, Z. Hu, C. Peng, L. Zhang, N. Wang, F. Wang, Y. Xia, S. Zhang, E. Hu and J. Luo, *Proc. Natl. Acad. Sci. U. S. A.*, 2024, **121**, e2309981121.
37 K. Qiu, G. Ma, Y. Wang, M. Liu, M. Zhang, X. Li, X. Qu, W. Yuan, X. Nie and N. Zhang, *Adv. Funct. Mater.*, 2024, **34**, 2313358.
38 Y. Liu, Z. Qin, X. Yang, J. Liu, X.-X. Liu and X. Sun, *ACS Energy Lett.*, 2022, **7**, 1814–1819.
39 W. Zhang, Y. Dai, R. Chen, Z. Xu, J. Li, W. Zong, H. Li, Z. Li, Z. Zhang and J. Zhu, *Angew. Chem., Int. Ed.*, 2023, **62**, e202212695.
40 Q. Gou, H. Luo, Q. Zhang, J. Deng, R. Zhao, O. Odunmbaku, L. Wang, L. Li, Y. Zheng and J. Li, *Small*, 2023, **19**, 2207502.
41 S. Wang, Y. Ying, S. Chen, H. Wang, K. K. K. Cheung, C. Peng, H. Huang, L. Ma and J. A. Zapien, *Energy Storage Mater.*, 2023, **63**, 102971.
42 Y. M. Li, W. H. Li, X. Y. Zhang, Y. Z. Tang, Z. M. Liu, J. P. Zhang and X. L. Wu, *Adv. Funct. Mater.*, 2025, **35**, 2420446.
43 R. Chen, W. Zhang, Q. Huang, C. Guan, W. Zong, Y. Dai, Z. Du, Z. Zhang, J. Li and F. Guo, *Nano-Micro Lett.*, 2023, **15**, 81.

44 C. Huang, X. Zhao, Y. Hao, Y. Yang, Y. Qian, G. Chang, Y. Zhang, Q. Tang, A. Hu and X. Chen, *Energy Environ. Sci.*, 2023, **16**, 1721–1731.
45 P. Xiao, H. Li, J. Fu, C. Zeng, Y. Zhao, T. Zhai and H. Li, *Energy Environ. Sci.*, 2022, **15**, 1638–1646.
46 S. Hsieh, T. Matsumoto, M. Batzill and B. E. Koel, *Phys. Rev. B: Condens. Matter Mater. Phys.*, 2003, **68**, 205417.
47 J. Pstruś, Z. Moser and W. Gąsior, *Appl. Surf. Sci.*, 2011, **257**, 3867–3871.
48 J. Dutkiewicz and W. Zakulski, *Bull. Alloy Phase Diagrams*, 1984, **5**, 284–289.
49 M. Abdallah, *Corros. Sci.*, 2003, **45**, 2705–2716.
50 S. Hu and W.-X. Li, *Science*, 2021, **374**, 1360–1365.
51 Z. W. Seh, J. Kibsgaard, C. F. Dickens, I. Chorkendorff, J. K. Nørskov and T. F. Jaramillo, *Science*, 2017, **355**, eaad4998.
52 P. Quaino, F. Juarez, E. Santos and W. Schmickler, *Beilstein J. Nanotechnol.*, 2014, **5**, 846–854.
53 S. Trasatti, *J. Electroanal. Chem. Interfacial Electrochem.*, 1972, **39**, 163–184.
54 M. Zhou, S. Guo, J. Li, X. Luo, Z. Liu, T. Zhang, X. Cao, M. Long, B. Lu, A. Pan, G. Fang, J. Zhou and S. Liang, *Adv. Mater.*, 2021, **33**, 2100187.
55 X. Liu, Y. Guo, F. Ning, Y. Liu, S. Shi, Q. Li, J. Zhang, S. Lu and J. Yi, *Nano-Micro Lett.*, 2024, **16**, 111.
56 W. Du, J. Yan, C. Cao and C. C. Li, *Energy Storage Mater.*, 2022, **52**, 329–354.
57 Y. Yuan, Z. Li, R. Deng, S. D. Pu, M. Walker, M. Cai, F. Wu, P. G. Bruce and A. W. Robertson, *Energy Environ. Sci.*, 2025, **18**, 5610–5621.
58 R. Yao, Y. Zhao, L. Wang, C. Xiao, F. Kang, C. Zhi and C. Yang, *Energy Environ. Sci.*, 2024, **17**, 3112–3122.
59 S. Chang, J. F. F. Gomez, S. Katiyar, G. Morell and X. Wu, *J. Am. Chem. Soc.*, 2023, **145**, 24746–24754.
60 Z. Lin, D. Li and Y. Zou, *J. Energy Storage*, 2023, **74**, 109386.
61 B. Shh and G. Ee, USA, 1999.
62 Z. Hu, F. Zhang, Y. Zhao, H. Wang, Y. Huang, F. Wu, R. Chen and L. Li, *Adv. Mater.*, 2022, **34**, 2203104.
63 Y. Wang, Y. Zhang, H. Ye, M. Wei, Y. Gu, K. Hu, S. Qu, R. Wu, X. Li and J. Zhang, *Small*, 2025, **21**, e09465.
64 J. Li, Z. Guo, J. Wu, Z. Zheng, Z. Yu, F. She, L. Lai, H. Li, Y. Chen and L. Wei, *Adv. Energy Mater.*, 2023, **13**, 2301743.
65 Q. Zhao, W. Liu, X. Ni, H. Yu, C. Zhang, B. Wang, L. Jiang, H. He, Y. Chen and L. Chen, *Adv. Funct. Mater.*, 2024, **34**, 2404219.
66 R. Wang, J. Zhu, M. Yang and Z. Niu, *Angew. Chem.*, 2025, **137**, e202501327.
67 Y. Yu, P. Zhang, W. Wang and J. Liu, *Small Methods*, 2023, **7**, 2300546.
68 S. Zheng, Y. Wang, B. Luo, L. Sun, G. Duan, J. Huang and Z. Ye, *Chem. Eng. J.*, 2023, **473**, 145313.